Journal of Operation and Automation in Power Engineering

Vol. XX, No. XX, Dec. 2022, Pages: XXXX (Proofed)

http://joape.uma.ac.ir

Research Paper

An Inductively Coupled Bidirectional DC-DC Converter With a Non-Pulsating Input Current for Renewable Energy Systems Energy Storage

Mohamad Reza Banaei *, *Mohamad Golmohamadi* , and *Hadi Afsharirad*

Department of Electrical Engineering, Azarbaijan Shahid Madani University, Tabriz, Iran.

Abstract— *The present study proposes a bidirectional DC-DC converter (BDC) that uses a non-isolated coupled-inductor (NI-CI). This converter can transfer power bidirectionally between the DC bus of a microgrid, supplied by PV or other renewable sources and energy storage system. The device exhibits a high voltage conversion ratio while using a few components. The converter applies the input inductance as a current ripple filter and uses a CI configuration to enhance the gain in boost mode. Also, the turns ratio of a coupled inductor is implemented to enhance the voltage conversion ratio to lower voltage stress. In addition, the converter's operation is more efficient considering its soft-switching advantages. The duty cycle control is applied to generate the desired voltage on both sides of the converter by controlling the corresponding power switch. It is worth noting that the low-voltage side current ripple is not significant. Besides, the results show an increase in voltage gain throughout boost mode and a decrease in voltage gain in the buck mode. Furthermore, the converter is mathematically studied in the following, and a PID converter is designed to illustrate the converter's stability. Finally, the practicality of the proposed NI-CI-BDC structure was validated by incorporating experimental results from a 200-watt prototype.*

Keywords—Optimal load distribution, decision theory with information gap, uncertainty, wind farm.

NOMENCLATURE

Parameters

C_1, C_2 and C_H Capacitors
D_1 and D_2 Antiparallel diodes of the power switches S_1 and S_2
I_{in} L_{in} inductor current (low voltage side current)
L_k, L_m Coupled inductor leakage and magnetizing inductances
L_p, L_{s1} and L_{s2} Coupled indutor total primary inductance, second and third windings inductances
L_{in} Low voltage side inductor
$V_{Lp,S1on}, V_{Lp,S1off}$ The voltage across the primary side of the coupled inductor during the on and off states of S_1
Cs Switch snubber capacitor
D Duty cycle
M The voltage ratio of the converter (V_H/V_L)
n The turn ratio of the coupled inductor (Ns/Np)
VL, VH The source voltages on the Low voltage and high voltage sides

1. INTRODUCTION

Bidirectional DC-DC structures have been extensively integrated into various domains, including uninterruptible power supply systems, microgrids, renewable energy sources, and electric transportation [1, 2]. These applications require batteries and a bidirectional converter. The needed voltage range in the applications varies depending on the converter's intended use. Batteries are essential components in renewable energy and microgrid applications [3]. Photovoltaic panels are one example of a renewable energy source generating a voltage output on the lower end. Consequently, a step-up converter and a step-down converter are essential for high- and low-voltage applications, respectively. To this end, a bidirectional DC converter is recommended [4]. Two types of bidirectional converters with high voltage ratios are isolated and non-isolated, each with distinctive merits and demerits. The performance of these converters is optimized using the bidirectional DC-DC converters with higher voltage gains while simultaneously fulfilling additional requirements, such as providing a higher power output and reducing voltage stress on semiconductor components [5]. Interleaved structures effectively reduce the voltage stress experienced by the semiconductor components in bidirectional DC converters. The interleaving of the topology leads to a notable decrease in the voltage stress the semiconductor encounters. The conventional buck-boost architectures represent the fundamental non-isolated DC converter topologies that can perform their duties in both the buck and boost modes. Despite this, conventional buck-boost converters exhibit excessive voltage stress on the switching components and restricted output voltage ratios. Implementing auxiliary circuits based on coupled inductors [6, 7] has facilitated the achievement of soft switching in the conventional buck-boost DC converter. Thus, the magnitude of stress encountered by the switches has declined. In [8–10], buck-boost converters with substantial voltage gain are represented. Besides, several DC-DC converters utilizing coupled inductors have been proposed [11–14].

However, the low-voltage side component of the converters

Received: 23 Apr. 2024
Revised: 05 Aug. 2024
Accepted: 09 Aug. 2024
*Corresponding author:
E-mail: m.banaei@azaruniv.ac.ir (M. Banaei)
DOI: 10.22098/joape.2024.14945.2142

is more susceptible to higher amounts of current stress than the other side components. In addition, the coupled inductors' leakage inductances cause the switches to have hard switching and excessive voltage spikes [12], thereby decreasing the converter's efficiency. Integrating the SEPIC-based structure into the buck-boost converter and employing two coupled inductors [13, 14] allows for developing bi-directional DC-DC converters that are soft-switched and exhibit minimal input current variations on the low voltage side. Using the SEPIC-based design enables the implementation of the buck-boost converter. The study Ref. in [15] explores integrating rooftop solar panels with a DC microgrid. This article proposes a high-gain DC-DC converter for solar systems that connects lower-voltage photovoltaic panels to a network with greater voltage. Ref. [16] describes another novel bidirectional DC-DC converter.

In contrast to modern converters, the mentioned converter features four power switches exposed to higher voltage stress than the proposed converter. A reduced ratio of output voltage is also evident. The Switched-Capacitor Bidirectional Converter (SCBC) is a commonly employed technology in electric vehicles. This converter leverages synchronous rectification to carry out the on-and-off operations effectively. According to [17], the SCBC demonstrates enhanced power conversion efficiency owing to its proficient use of power switches and not requiring additional components. A newly developed bidirectional DC-DC converter without an auxiliary switch is presented in Ref. [18]. This converter applies zero-voltage switching and does not require any additional components. This topology incorporates a three-winding coupled inductor. However, the voltage gain for the boost state is still rather low and is equivalent to that of a conventional boost converter. Ref. [19] discusses a non-isolated bidirectional DC-DC converter utilizing partial power processing. It combines a direct power flow path with the converter, enhancing energy efficiency and offering high energy density, simplicity, compact size, and low electromagnetic interference. This converter is ideal for bidirectional energy management in applications like photovoltaics, fuel cells, and supercapacitor storage, capable of both increasing and decreasing input voltage and supporting bidirectional current flow. However, this topology has the drawback of a low output voltage ratio. Ref. [20] proposes a coupled-inductor-based DC-DC converter with high step-up and step-down capabilities, designed for electric vehicle (EV) applications. A two-winding coupled inductor enhances the voltage gain in both directions, while low current ripple at the low-voltage port makes it ideal for renewable energy sources. The converter's efficiency is competitive due to its minimal component count. Additionally, the use of only three bidirectional switches with low voltage stress reduces both cost and volume. Despite the mentioned advantages of the bidirectional Ref. converter structure [20], it suffers from limitations such as increased number of switches and high stress on switches, along with a low voltage gain. Addressing these issues, several new boost converter topologies have been proposed in Refs. [21–23]. Ref. [24] introduces a nonisolated hybrid bidirectional DC-DC converter (NHBC) with high step-up and step-down voltage conversion ratios. It features reduced voltage and current stresses on semiconductor devices and decreased inductor current ripples, making it energy-efficient and suitable for applications like electrified aviation power systems. The NHBC uses bidirectional switch-diode capacitor and coupled inductor cells, operating in continuous conduction mode, to improve voltage conversion and reduce current ripples and device stresses. An innovative bidirectional DC-DC converter with a high voltage conversion ratio and the ability to eliminate input current ripple is proposed in Ref. [25]. By utilizing two coupled inductors and a switched-capacitor circuit, the converter achieves efficient voltage conversion. Adjustment of the coupled inductors' magnetizing inductance values allows for the cancellation of input current ripple at the low voltage side, tailored to a specific duty cycle. The converter optimizes switch current stresses by splitting the input current across the primary winding of the coupled inductors. It features five switches with internal diodes to facilitate bidirectional power flow, supporting both boost and buck operations effectively.

The present study introduces a novel bidirectional DC-DC topology that achieves a high voltage ratio. The converter is set up as a boost converter on the low-voltage side and a buck converter on the high-voltage side. Integrating an inductor on the low-voltage side of the converter declines the input current fluctuation. Moreover, including a coupled inductor in its setup leads to achieving a high voltage ratio. Utilizing the structure in a parallel and interleaved manner can enhance the output power. Additionally, the converter demonstrates the advantages of decreased voltage stress on switches and a minimal number of components. In this respect, a coupled inductor is used to enhance the voltage gain by leveraging its turn ratio, thereby expanding the output voltage gain.

1.1. Proposed converter operation

Fig. 1 depicts the proposed converter circuit structure and the application of this converter in a sample PV- Battery DC microgrid system. The converter comprises one coupled inductor with three windings and an input inductor that assists in reducing ripple in the input current. Soft switching conditions can be achieved using a resonant tank containing L_2 and C_2. In working modes, the resonant inductor L_2 charges and discharges the parallel snubber capacitor of switch S_1 to achieve the ZVS condition for this power switch. In addition, the secondary side of the coupled inductor in the resonant loop is connected to the capacitor C_2, which prevents DC from passing through it. The coupled inductor has a turn ratio of Ns/Np, where L_k denotes its leakage inductance, and L_m shows its magnetizing inductance. In addition, the value of the coupling coefficient K is expressed as $K = \sqrt{L_m/(L_m + L_k)}$. In addition, a pair of power switches are employed to transfer power between the low-voltage and high-voltage sides in both directions. Capacitors C_1 and C_H function to conserve energy and transfer it to the high-voltage side output. In addition, the amalgamation of L_{in}, C_1, and C_H results in a low-pass filter that decreases the input current ripple. The proposed configuration designates V_L as the low-voltage terminal and V_H as the converter's high-voltage terminal.

In this converter, switch S_1 has PWM pulses, and switch S_2 acts as a diode to transfer the energy from V_L to V_H. Meanwhile, to transfer power in the opposite direction, the switch S_2 has PWM pulses, and the switch S_1 acts as a diode.

2. The proposed structure's operational characteristics

Fig. 2 illustrates the essential waveforms of the step-up mode. In boost mode, the proposed working modes for the converter consist of five modes.

2.1. Step-up mode

In step-up mode, switch S_1 has pulses created by pulse width modulation, whereas switch S_2 works as a diode. Below, the modes 1 to 5 are described.

Mode 1: This mode is depicted in Fig. 3-(a). During this time span, the body diode of the switch (S_1) is activated such that the current through the power switch S_1 is zero before its activation. Therefore, the ZCS condition for the S_1 turn-on is provided. The capacitor C_1 is discharged to the output, while the capacitor C_H is charged at the output. During this time, the magnetizing inductance current (I_{Lm}) is rising.

Mode 2: Fig. 3-(b) shows the characteristics of the circuit in Mode 2. The power switch (S_1) is activated in this mode when the condition ZVZCS is met. In Mode 1, the diode provides the ZCS condition, and in Mode 5, zero voltage is obtained by discharging

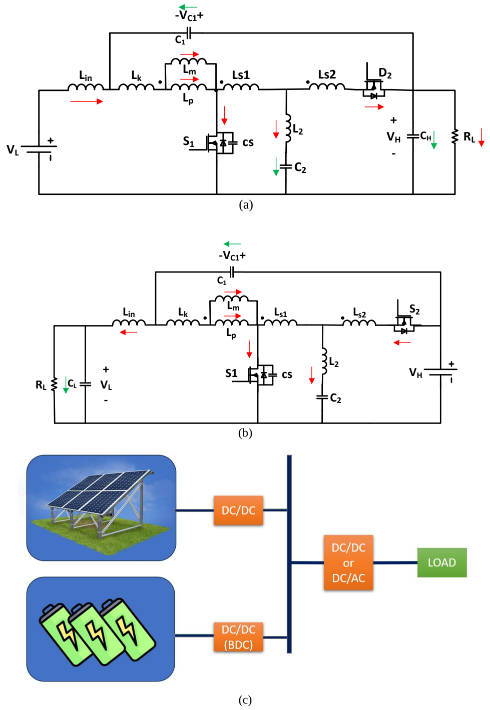

Fig. 1. The fundamental circuit of the proposed bidirectional DC-DC converter a) In the boost state, b) In the buck state, and c) The schematic of a PV-battery DC microgrid with proposed bidirectional DC-DC converter (BDC).

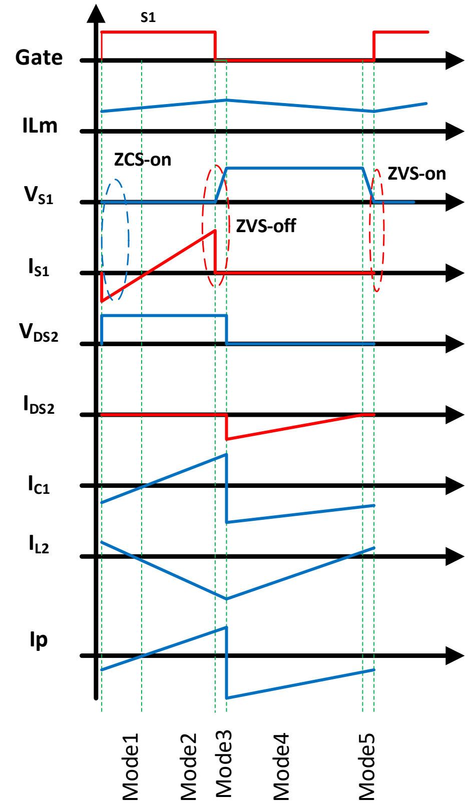

Fig. 2. Principal waveforms of boost mode.

the parallel snubber capacitor C_s. In addition, capacitor C_1 is in a charged state, and capacitor C_0 provides power to the load that is being output. Besides, the current of the magnetizing inductance (I_{Lm}) continues to increase with time.

Mode 3: During this mode, as depicted in Fig. 3-(c), the parallel capacitor $S_1(C_s)$ charges slowly. In ZVS mode, therefore, the power switch (S_1) is turned off and magnetizing inductance remains magnetized until the mode concludes.

Mode 4: During the zero-voltage switching (ZVS) state, the power switch (S_1) is fully off in Mode 4, as shown in Fig. 3-(d). The output load receives power from the diode D_{S2} and the secondary side of the coupled inductor. Also, capacitor C_1 is discharged, and capacitor C_H is charged at the same time. Another fascinating finding is that the electric current passing through the magnetizing inductance of the coupled inductor (I_{Lm}) declines significantly.

Mode 5) The final mode is depicted in Fig. 3-(e). In this mode, the parallel snubber capacitor of the switch (S_1) discharges to zero to achieve the ZVS situation necessary for the switch S_1 to be turned on. The capacitors C_1 and C_o discharge the output load. In addition, the magnetizing inductance current continues to decrease in this mode. This condition ends at the end of this time period.

2.2. Step-down mode

The essential waveforms of step-down mode are depicted in Fig. 4. During the buck state, the power switch S_2 receives PWM pulses, while the switch S_1 functions as a diode. This condition occurs in five different modes. Modes 1 through 5 are covered in the following lines.

Mode 1: Fig. 5-(a) presents this manner of operation in the first mode. During this time span, the body diode of switch S_2 is on. Thus, the current through the respective power switches is zero before turning on. The ZCS condition is therefore given for the power switch S_2 to be switched on; the capacitor C_1 is discharged; and the L_{in} inductor delivers energy to the output load. Also, during this mode, the output capacitor is charged. Furthermore, the magnetizing inductance is experiencing a decrease in current and demonstrating a negative direction.

Mode 2: Fig. 5-(b) represents the circumstances of the circuit in Mode 2. The S_2 power switch is activated when ZCS is met in this mode. The ZCS condition is given by the body parallel diode of S_2 at Mode 1. Moreover, the capacitor C_1 changes and the magnetizing inductance L_m continues demagnetizing.

Mode 3: In this state, as depicted in Fig. 5-(c), the power switch (S_2) on the high-voltage side is turned off. The circuit capacitor C_1 undergoes the charging process, while the inductor L_{in} and output capacitor CL provide power to the output load. The output voltage regards a drop in amplification due to the decreased turn ratio of the coupled inductor from the high voltage side to the low voltage side.

Mode 4: This mode maintains the critical power switch S_2 in the deactivated state, whereas the body diode of switch S_1 is activated. In this particular mode, the capacitor C_1, which was previously charged, is discharged.

Mode 5: In Fig. 5-(e), the body diode DS1 is turned off because of a change in the current direction of the resonant inductor L_2. Also, the S_2 switch has no pulses yet.

3. THE CONVERTER EVALUATIONS IN THE STEADY-STATE CONDITION

This section analyzes the significant mathematical parameters and the voltage stress experienced by power switches in the proposed converter.

3.1. Voltage ratio and stress of voltage on semiconductors

The present section focuses on the steady-state calculations of Modes 2 and 4 since most switching operations take place in these

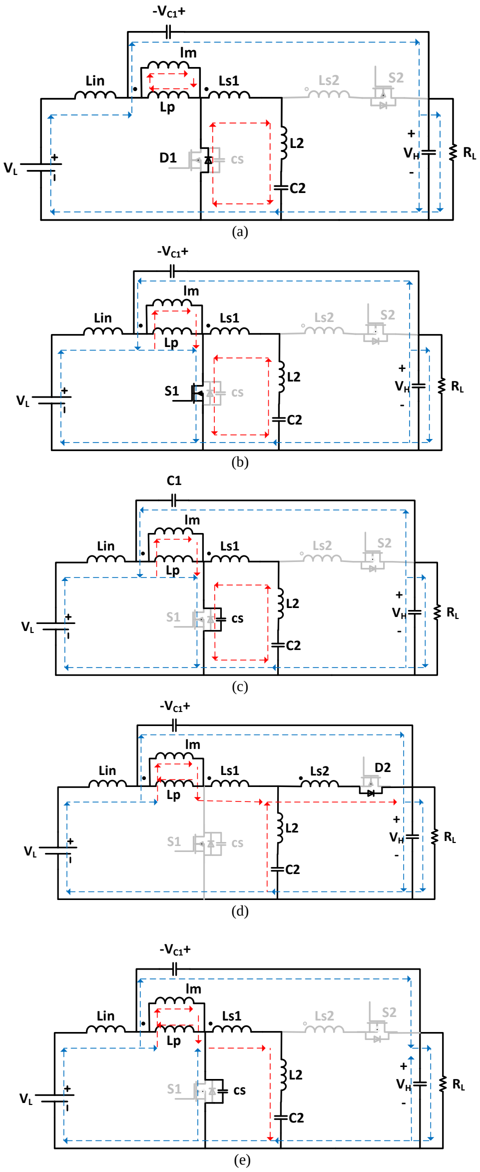

Fig. 3. The operational modes for the step-up operation: a) Mode 1, b) Mode 2, c) Mode 3, d) Mode 4, and e) Mode 5.

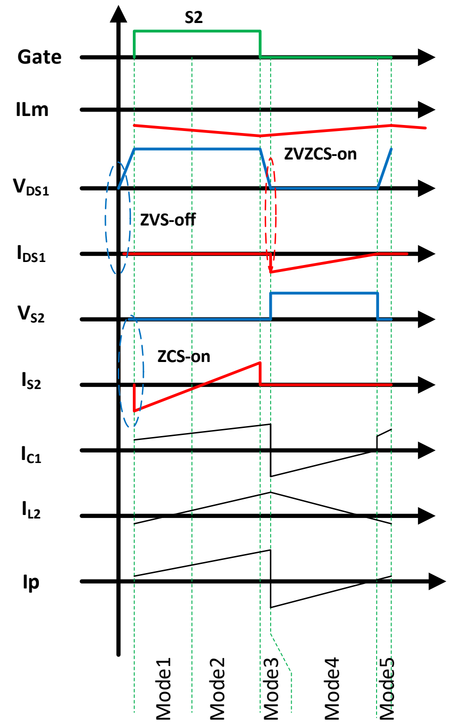

Fig. 4. Principal waveforms of buck mode.

modes. In contrast, the time intervals in the remaining modes are relatively brief, leading to neglecting some computations.

The proposed converter's input inductor (L_{in}) functions as a current filter, resulting in a limited current ripple. The KVL is constituted by the input inductor (L_{in}), input voltage source (V_L), and capacitors C_1 and C_2. In a state of steady equilibrium, the voltage across the inductor (L_{in}) is considered negligible due to the constant voltage present across the capacitors and input voltage. Furthermore, the capacitance values are deemed to be of sufficient magnitude to maintain a consistent voltage.

A mathematical analysis was provided to verify the voltage ratio of the proposed structure during the boost state of operation, with Modes 2 and 4 serving as the main operating modes. Nevertheless, the buck state equations will yield the identical V_L/V_H gain equation. Also, the consequence of leakage inductance (L_k) on the ratio of voltage and capacitor voltage leads to the following calculations. Here, it is assumed that the value of the coupling coefficient is K = Lm/(Lm+Lk) and L_m is the magnetizing inductance of the coupled inductor at its primary side: The voltage second equation for coupled inductor primary side inductance (L_P) is solved using Eqs. (1) and (2):

$$V_{Lp,S1on} = V_L \tag{1}$$

$$V_{Lp,S1off} = \frac{V_L - V_H}{1+2n} \tag{2}$$

where $V_{Lp,on}$ and $V_{Lp,off}$ denote the voltage values on the main side of the coupled inductor when the power switch S_1 is turned on and off, respectively. Also, n represents the ratio of the number of turns in the secondary winding to the number of turns in the primary winding. Finally, V_L and V_H represent the low- and high-voltage sources, respectively.

The voltage gain can be calculated by applying the voltage-second rule on the primary side of the coupled inductor (L_P), as shown below:

$$V_H/V_L = \frac{2KnD+1}{1-D} \tag{3}$$

Also, the voltage on the capacitor C_1 can be obtained when the KVL rule turns off the switch S_1 (Eq. (4)):

$$+Vc_1 + V_{Lp} + 2V_{L\,\mathrm{sec}} = 0 \rightarrow Vc_1 = \frac{(2nK+1)D}{1-D} V_L \tag{4}$$

where V_{Lsec} represents the voltage across the secondary coil of the coupled inductor. Fig. 6 depicts the proposed converter's voltage ratio curves, showcasing several coupling coefficient values. The performance of the proposed converter is somewhat affected by the amount of the transformer's leakage inductance. In addition, the influence of the leakage inductance on the voltage gain is nonsignificant.

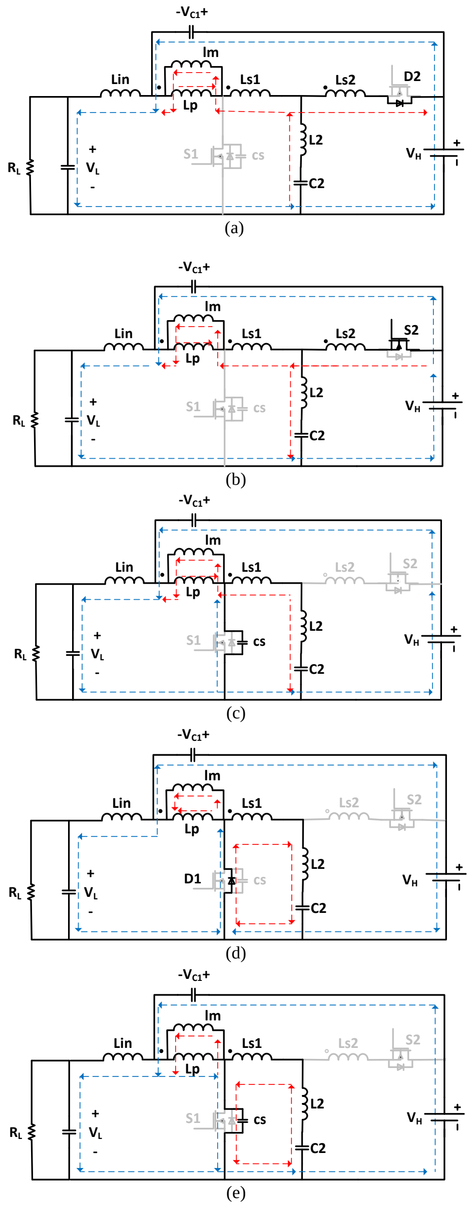

Fig. 5. The operational modes for the step-down operation: a) Mode 1, b) Mode 2, c) Mode 3, d) Mode 4, and e) Mode 5.

3.2. Design considerations

This section addresses the design procedure for the circuit inductors and capacitors.

A) Voltage stress

The voltage stress existing on the major power switches $S_1(V_{S1})$ to $S_3(V_{S3})$ is calculated by the following equations:

$$V_{S1,\max} = \frac{1}{1-D} V_L, V_{S2,\max} = \frac{2n+1}{1-D} V_L \tag{5}$$

B) Magnetizing inductance

According to the voltage-current equation of inductor, from Mode 2 of boost mod, and by replacing V_L from Eq. (8), the value of magnetizing inductor (L_m) can be calculated as follows:

$$L_m \geq \frac{V_H(1-D)D}{2f(1+2nD)\Delta i_{Lm}} \tag{6}$$

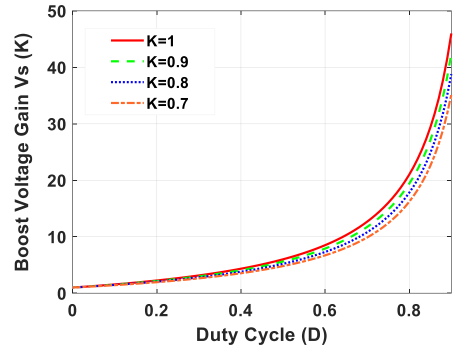

Fig. 6. Proposed converter boost voltage gain with respect to the coupling coefficient (K), n=2.

The variable f represents the converter's switching frequency, while Δi_{Lm} denotes the specified current ripple of the magnetizing inductor current.

C) ZVS condition considerations

To achieve ZVS operation for the proposed converter, the inductor L_2 must possess sufficient energy to facilitate the charging and discharging of the snubber capacitor C_s. Thus, we have:

$$\frac{1}{2} L_2 \left(\frac{I_{in}}{n}\right)^2 \geq C_s \left(\frac{V_L}{1-D}\right)^2 \tag{7}$$

4. Averaged Model Analysis

In this section, the averaged model analysis is performed, followed by figuring out the converter's transfer function for changes in output voltage vs. changes in the duty cycle. In addition, the MATLAB programming software was used to develop a PID controller with values ideal for the system. Moreover, the converter's transfer function and the Bode diagram's step response are presented.

To derive the small signal equations for the proposed converter, the primary equations of the converter in both the on and off states of the power switch are first calculated. Next, perturbations are applied to these equations. After linearizing and removing second-order and higher terms, the transfer function of the converter can be determined.

When S_1=1 (S_1 is on), we have:

$$\begin{cases} L_p \frac{di_{Lp}}{dt} = V_L \\ C_1 \frac{dV_{C1}}{dt} = i_{Lp} - i_{in} \\ Co \frac{dV_H}{dt} = -\frac{V_H}{R} - C_1 \frac{dV_{C1}}{dt} \end{cases} \tag{8}$$

And when S_1=0 (S_1, off), it can be written as:

$$\begin{cases} L_p \frac{di_{Lp}}{dt} = \frac{V_L - V_H}{2n+1} \\ C_1 \frac{dV_{C1}}{dt} = i_{Lp} - i_{in} \\ Co \frac{dV_H}{dt} = -\frac{V_H}{R} + i_{in} \end{cases} \tag{9}$$

Where I_{in} is the input current on the low voltage side. In this section, the perturbation is applied as follows:

$$\begin{aligned} &< i_{Lp} >= I_{Lp} + \hat{i}_{Lp}, < V_L >= V_L + \hat{v}_L, \\ &< V_{C1} >= V_{C1} + \hat{v}_{C1}, < I_{in} >= I_{in} + \hat{i}_{in}, \\ &< V_H >= V_H + \hat{v}_H, d = D + \hat{d} \end{aligned} \tag{10}$$

Consequently, the transfer function establishing a relationship between the duty-cycle variations and the output voltage of the converter can be derived as follows after the linearization process:

$$\frac{\hat{V}_H}{\hat{d}} = \frac{V_H+2nV_L+2Dn^2RV_L+DnRV_H-nI_{in}lpR\times s-2I_{in}lp\times n^2R\times s}{lp\times s-D+nDR+2nlps-D^2nR+C_H\times lp\times Rs^2+2C_H\times nlpRs^2+1} \quad (11)$$

According to Fig. 7, the proposed DC-DC converter has been analyzed to determine its stability parameters, yielding the following results: Gain Margin: 10.9 dB, Phase Margin: 60 degrees, Gain Crossover Frequency: ∞ rad/s.

These stability parameters indicate that the DC-DC converter is designed with a robust stability margin. A gain margin of 10.9 dB suggests that the system can tolerate a gain increase of up to 10.9 dB before becoming unstable. This margin is within the generally recommended range of 10-20 dB, ensuring that the converter can handle variations in system gain without risking instability.

A phase margin of 60 degrees indicates a high level of phase stability, as it is well within the typical range of 45-60 degrees. This margin means the system can tolerate additional phase lag up to 60 degrees before reaching the brink of instability. Such a phase margin enhances the converter's robustness to component variations and changes in operating conditions, contributing to its reliable performance.

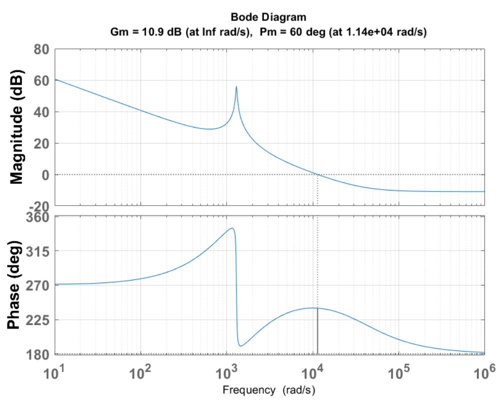

Fig. 7. Bode diagram representing the proposed converter transfer function.

In this section, a PID controller for the proposed converter is designed. K_P = 0.0294, K_I = 19.6, and K_D = 1.1e-5 are the coefficients for the PID controller.

Fig. 8-(a) illustrates the step response of the closed-loop system. The system exhibits a settling time of 3 milliseconds and a maximum overshoot of approximately 16 percent. This step response is derived using the actual parameter values of the converter as specified in Table 2.

The proposed converter can act as a storage system manager, either supplying power to the DC microgrid or charging the battery when the microgrid has enough power to meet DC load demands and charge the battery. The closed-loop control system block diagram is shown in Fig. 8-(b). In this system, the power requirement for the grid can be specified as an input, and the direction of power flow can be set to zero or one. An input of zero indicates that the grid should be powered by the battery storage, while an input of one indicates that the battery can be charged from the grid power using a constant current, constant voltage (CC/CV) method or any other suitable charging method. Additionally, the charge voltage and current can be configured through the CC/CV controller inputs.

5. Performance Comparison

This part provides a comparative assessment of the proposed bidirectional structure and six other converters that have been recently presented. The proposed converter exhibits identical features to those of other comparative converters. Table 1 comprehensively categorizes and compares the criteria that have

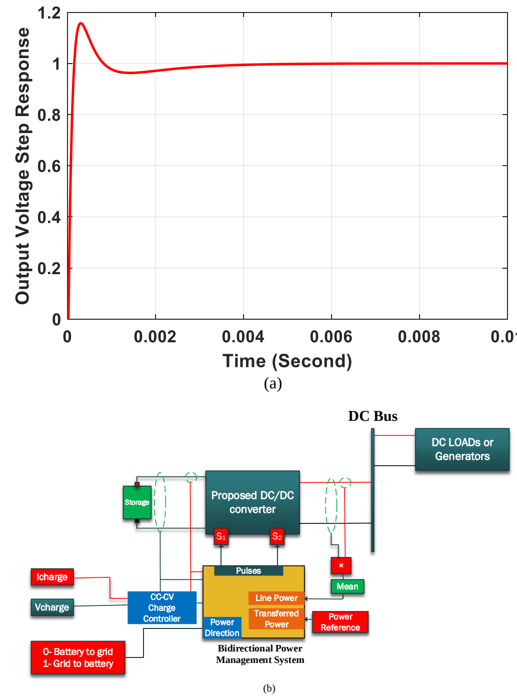

Fig. 8. The proposed converter control system, a) Proposed structure step-response in the presence of PID controller, b) the block diagram of the system control schematic.

been employed. Fig. 9-(a) also illustrates a comparative analysis of the conversion ratio between the proposed and previously developed structures. Furthermore, Fig. 9-(b) compares the normalized voltage stress across various semiconductors. The results show that the proposed converter benefits lower voltage stress, resulting in higher efficiency. According to the mentioned table and figures, the proposed structure offers advantages in terms of a reduced count of passive and active components by considering a very high boost gain. Thus, it leads to easy control, simplified regulation of power switches, and lower total voltage stress by increasing the boost voltage gain. Furthermore, the proposed converter uses a single switch (S_1) to increase voltage gain significantly and offers superior efficiency compared to alternative designs.

6. Analysis of Power Loss and Efficiency

The efficiency of the bidirectional converter under consideration is verified by establishing the following parasitic resistances: Here, rds denotes the resistance in the ON state of the switch; R_{Lin} and R_{Lm} represent the ESRs for inductors L_{in} and L_m; and r_{C1}, r_{C2}, and r_{CH}, respectively, represent the ESRs for capacitors C_1, C_2, and C_H. Furthermore, the transient voltage exhibited by the capacitors and inductors is also considered.

The conduction loss (P_{rds}) of the switch S_1 or S_2 is calculated as follows:

$$P_{S1,2} = R_{ds}({I^2}_{S1,2}) \quad (12)$$

The conduction losses of inductors L_{in} and L_m (P_{Lin}, P_{Lm}) can be achieved as follows:

$$P_{Lin} = R_{Lin}(\frac{2nd+1}{1-d})^2 I_H^2,\ P_{Lp} = R_{Lp}n^2 I_H^2 \quad (13)$$

where I_H is the high voltage side electrical current. The losses of capacitors C_1 and C_H (i.e., P_{C1} and P_{CH}, respectively) can be derived as:

Table 1. The proposed converter compared with other structures.

(n=2, $V_L = 48V$, $V_H = 300V$	S^*	D^*	TIC/W^*	C^*	QTY^*	Voltage ratio	Normalized Switch voltage Stress	TSVS	Soft switching	Efficiency (%) @ 200W	
										Boost	Buck
Proposed	2	0	3/3	3	8	$\frac{1+2nD}{1-D}V_L$	$\frac{2n+M}{2n+1}$, $2n+M$	587V	ZVS-ZVZCS	93.4%	94.5%
Ref. [15]	4	0	2/0	3	9	$\frac{V_L}{1-D}$	M	1200V	×	87.7%	87.1%
Ref. [16]	4	0	2/0	3	9	$\frac{2}{1-D}V_L$	M, 2M	900V	×	93.8%	93.6%
Ref. [17]	5	0	2/0	5	12	$\frac{3}{1-D}V_L$	M/3	520V	×	90.2%	89.2%
Ref. [18]	2	2	1/3	1	6	$\frac{V_L}{1-D}$	M	1200V	ZVS-ZVZCS	92.1%	94.1%
Ref. [20]	3	0	2/2	3	8	$\frac{D+1-(1/n)}{(1-D)(1-1/n)}$	M	900V	×	93.5%	91.2%
Ref. [24]	4	0	2/2	4	10	$\frac{1+3D}{1-D}$	$\frac{2M}{(4-3d)}$	960V	ZVS	93.6%	97.8%
Ref. [25]	5	0	2/2	3	10	$\frac{1+N(1-D)}{D(1-D)}$	M, M/2	1200V	×	92.8%	91.5%

***S:** Switches count, **D:** Diodes count, **TIC/W:** Total inductors count/coupled inductor windings, **C:** Capacitors count, **QTY:** Overall quantity of elements, and **TSVS:** Total semiconductors voltage stress

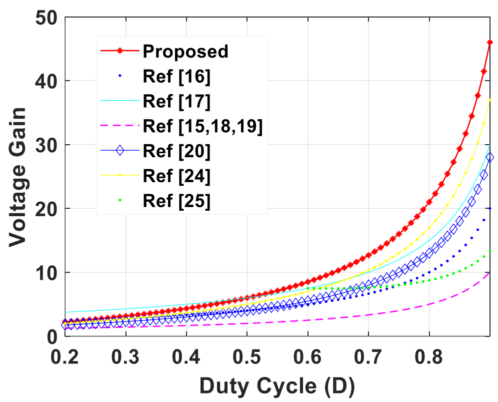

(a)

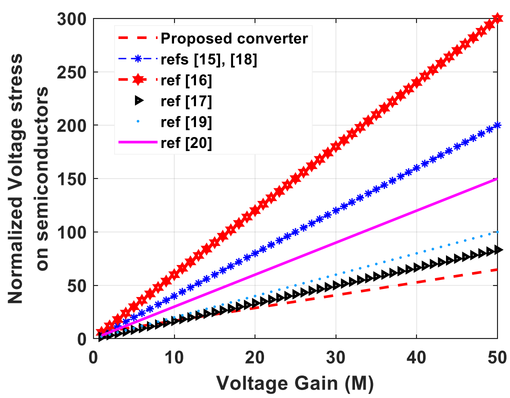

(b)

Fig. 9. A comparison between the proposed converter and other existing topologies: a) Comparative analysis of the voltage ratio and b) Normalized voltage stress comparison.

$$P_{rC1,CH} = R_{C1,CH}\left(\frac{M(M-1)V_L}{R}\right) \tag{14}$$

The expression for the total loss of the proposed converter, denoted as P_{Loss}, is as follows:

$$P_{Loss} = P_{switch} + P_{rC1,Co} + P_{Lin,Lm} \tag{15}$$

The attainment of efficiency for the suggested converter can be realized through Eq. (16):

Table 2. Specifications and component values of implemented circuit.

Parameter	Value
Output power	200W
V_L	48
V_H	300V
Switching frequency	39kHz
Switches (S_1 and S_2)	(S_1:IRFP260N), (S_2:FQA10N80)
Magnetizing inductance	560μH
Gate Driver	Isolated transformer driver
Duty-Cycle	51%
Turn ratio	2 (Ns/Np)
PWM-IC	TL494
L_{in}	100μH
L_2	150μH
$C_{1,o}$	100μF
C_s	10nF
C_2	2.2μF, 450V polyester

$$eff = \frac{P_{output}}{P_{output} + P_{Loss}} \tag{16}$$

7. Experimental Results

A 200-watt prototype (Fig. 10) was implemented to test the performance of the bidirectional converter following the theoretical analysis. Table 2 shows the specifications and components used in the process of implementing the prototype.

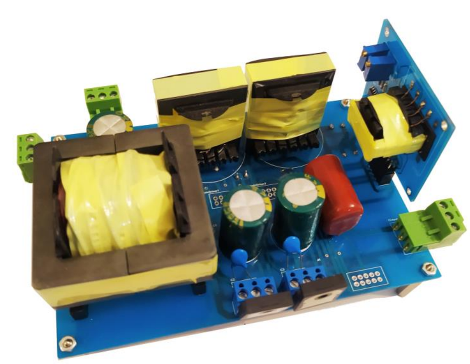

Fig. 10. Illustration of implemented proposed structure.

Several of the most important experimental results for the boost state of the converter are depicted in Fig. 11. This figure depicts (a) the high and low voltage side voltage waveforms, (b) the switch S_1 voltage and current waveforms, (c) the switch S_2 voltage waveform, d) C_1 voltage waveform, and e) the dynamic response of the proposed converter by implementing a step change

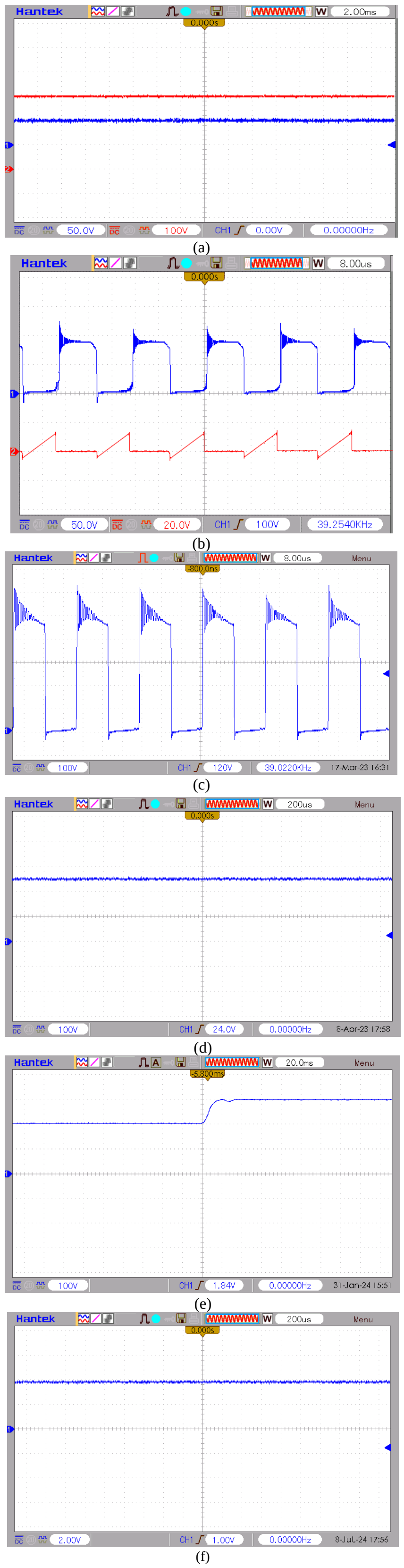

Fig. 11. Main experimental boost state waveforms for V_L= 48V and V_H=300V: a) V_H and V_L, b) S_1-voltage (50 V/div) and current (20A/div), c) S_2-Voltage, d) C_1 voltage waveform, e) Voltage step from V_H = 200V to 300V, and f) L_{in} inductor current (2A/div).

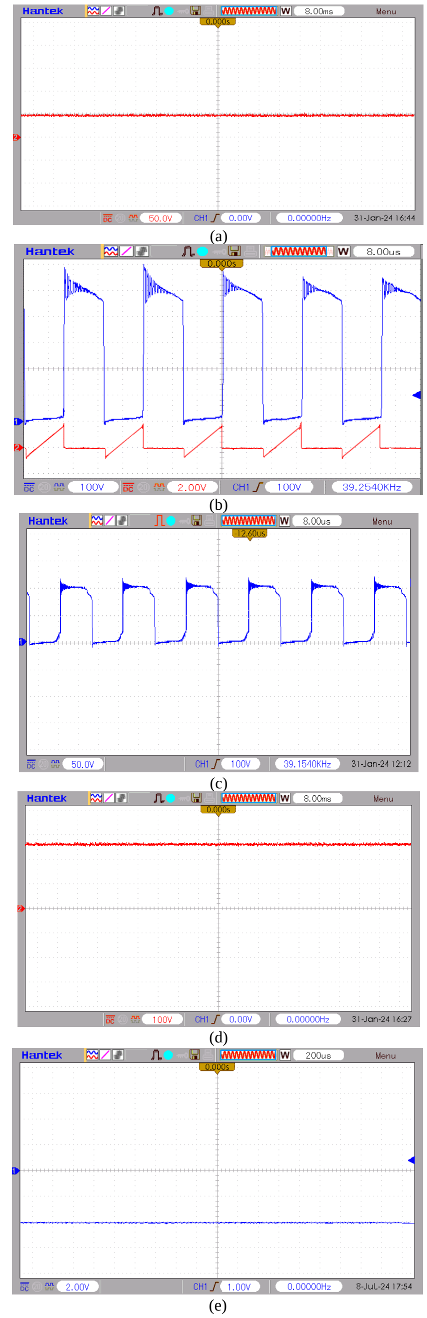

Fig. 12. Main experimental buck state waveforms for V_H=300V and V_L=48V: a) V_L waveform, b) S_2-voltage (50V/div) and current (2A/div), c) S_1-Voltage, d) C_1 voltage waveform, and e) L_{in} inductor current (2A/div).

from 200V to 300V output during the boost mode of operation. However, only the boost state output waveforms were given due to the similarity of voltage waveforms for the buck and boost states with the same V_H and V_L.

According to Eq. (4) and by considering the parameter values in Table 2, for capacitor voltage V_{C1}, we have:

$$Vc_1 = \frac{5 \times 0.51}{1-0.51}.48V \simeq 249.8V \tag{17}$$

Also, for voltage stress across switches S_1 and S_2, we that:

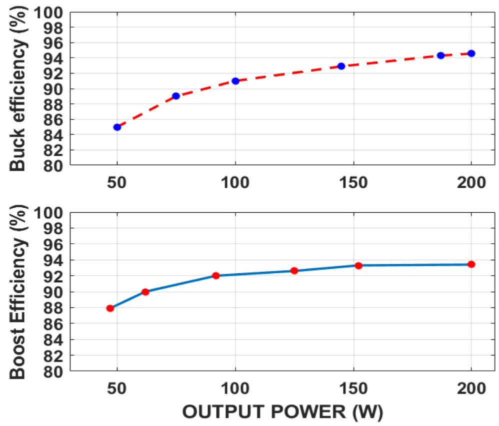

Fig. 13. The waveforms indicating the efficiency of the proposed converter.

$$V_{S1,\max} = \frac{1}{1-0.51}.48V \simeq 98V \tag{18}$$

$$V_{S2,\max} = \frac{5}{1-0.51}.48V \simeq 489.8V \tag{19}$$

According to Eq. (6) the minimum calue of magnetizing inductance for coupled inductor can be calculated as below:

$$L_m \geq \frac{300(1-0.51)0.51}{2\times 39000(1+2.04)\times 0.8} = 395.2\mu H \tag{20}$$

In the previous equation, the current ripple in L_m is considered to be 10% of the total current through this inductor. To achieve soft-switching for the proposed converter, the following equations must be applied for the snubber capacitor C_s and inductor L_2:

$$\begin{aligned} &\tfrac{1}{2}L_2(\tfrac{I_{in}}{n})^2 \geq C_s(\tfrac{V_L}{1-D})^2 \rightarrow \\ &0.5\times 150\times 10^{-6}\times 17.36 > 10\times 10^{-9}\times 8858 \rightarrow \\ &1.3\times 10^{-3} > 0.89\times 10^{-3} \rightarrow Passed \end{aligned} \tag{21}$$

The most important experimental waveforms of the buck converter are also depicted in Fig. 12. This figure shows (a) the V_L waveform, (b) the S_2 power switch voltage and current waveforms, (c) the S_1 power switch voltage, (d) the C_1 voltage waveform, and the current I_{Lin} on the low-voltage side.

Fig. 13 illustrates the efficiency curves of the proposed converter in both the buck and boost stages. According to the graph, the converter's efficiency at a load of 200-watt on the output stage for buck operation is 94.5%. In comparison, the efficiency of the boost stage is 93.4%.

8. CONCLUSION

The present study describes a new proposed bidirectional DC-DC topology that reduces voltage stress on its semiconductor components and achieves a high voltage gain. The study evaluated and conducted a mathematical analysis of the proposed structure. Also, an analysis was conducted on the small signal model of the converter, thereby deriving the transfer function that relates the output voltage to changes in the duty cycle. According to the modeled system, gain and phase margins of 10.9 dB and 60 degrees, respectively, confirm the stability of the converter. In addition, a PID controller was created using MATLAB software's PID-tune tools, and the step response of the closed-loop system was demonstrated. The converter's efficiency at a 200-watt load is 94.5% for buck operation and 93.4% for boost operation. Finally, a comparative analysis was conducted, followed by developing a 200-watt prototype to validate the functionality of the proposed converter.

REFERENCES

[1] M. R. Banaei and H. A. F. Bonab, "A high efficiency nonisolated buck–boost converter based on zeta converter," *IEEE Trans. Ind. Electron.*, vol. 67, no. 3, pp. 1991–1998, 2019.

[2] S. G. Sani, M. R. Banaei, and S. H. Hosseini, "Investigation and implementation of a common ground dc-dc buck converter with a novel control method for loss reduction in the converter," *IET Power Electron.*, 2024.

[3] M. R. Banaei, M. Golmohamadi, and H. Afsharirad, "A bidirectional high voltage ratio dc–dc topology for energy storage systems in microgrid," *IET Power Electron.*, vol. 17, no. 2, pp. 281–294, 2024.

[4] S. You, Z. Wang, and Y. Sun, "Charging strategy of an integrated onboard ev charger with a small intermediate capacitor," *CSEE J. Power Energy Syst.*, 2023.

[5] M. Yaqoob, K. H. Loo, and Y. Lai, "Extension of soft-switching region of dual-active-bridge converter by a tunable resonant tank," *IEEE Tran. Power Electron.*, vol. 32, no. 12, pp. 9093–9104, 2017.

[6] R. Rezaii, M. Nilian, M. Safayatullah, F. Alaql, and I. Batarseh, "Design and experimental study of a high voltage gain bidirectional dc-dc converter for electrical vehicle application," in *2022 IEEE Appl. Power Electron. Conf. Exposition*, pp. 2058–2063, IEEE, 2022.

[7] M. Banaei, H. Ajdar Faeghi Bonab, and N. Taghizadegan Kalantari, "Analysis and design of a new single switch non-isolated buck-boost dc-dc converter," *J. Oper. Autom. Power Eng.*, vol. 8, no. 2, pp. 116–127, 2020.

[8] Z. Yan, J. Zeng, W. Lin, and J. Liu, "A novel interleaved nonisolated bidirectional dc–dc converter with high voltage-gain and full-range zvs," *IEEE Trans. Power Electron.*, vol. 35, no. 7, pp. 7191–7203, 2019.

[9] C.-C. Lin, L.-S. Yang, and G. Wu, "Study of a non-isolated bidirectional dc–dc converter," *IET Power Electron.*, vol. 6, no. 1, pp. 30–37, 2013.

[10] F. G. Nimitti, J. C. Giacomini, and A. M. S. S. Andrade, "Dual-stacked bidirectional boost/buck dc–dc converter," *IEEE Trans. Ind. Electron.*, vol. 70, no. 9, pp. 8873–8882, 2022.

[11] Y.-T. Chen, Z.-X. Lu, and R.-H. Liang, "Analysis and design of a novel high-step-up dc/dc converter with coupled inductors," *IEEE Trans. Power Electron.*, vol. 33, no. 1, pp. 425–436, 2017.

[12] C.-M. Hong, L.-S. Yang, T.-J. Liang, and J.-F. Chen, "Novel bidirectional dc-dc converter with high step-up/down voltage gain," in *2009 IEEE Energy Convers. Congr. Exposition*, pp. 60–66, IEEE, 2009.

[13] F. Wu, S. Fan, X. Li, and S. Luo, "Bidirectional buck–boost current-fed isolated dc–dc converter and its modulation," *IEEE Trans. Power Electron.*, vol. 35, no. 5, pp. 5506–5516, 2019.

[14] M. R. Banaei and S. G. Sani, "Analysis and implementation of a new sepic-based single-switch buck–boost dc–dc converter with continuous input current," *IEEE Trans. Power Electron.*, vol. 33, no. 12, pp. 10317–10325, 2018.

[15] P. S. Kulasekaran and S. Dasarathan, "Design and analysis of interleaved high-gain bi-directional dc–dc converter for microgrid application integrated with photovoltaic systems," *Energies*, vol. 16, no. 13, p. 5135, 2023.

[16] B. Krishna, G. Lithesh, and V. Karthikeyan, "A novel high-gain bidirectional dc–dc converter for ev onboard charger applications," *Int. J. Circuit Theory Appl.*, vol. 50, no. 7, pp. 2531–2547, 2022.

[17] Y. Zhang, W. Zhang, F. Gao, S. Gao, and D. J. Rogers, "A switched-capacitor interleaved bidirectional converter with wide voltage-gain range for super capacitors in evs," *IEEE Trans. Power Electron.*, vol. 35, no. 2, pp. 1536–1547, 2019.
[18] N. A. Madiseh, E. Adib, and M. R. Amini, "A novel soft switching non-isolated bidirectional dc–dc converter without any extra auxiliary switch," *IEEE J. Emerging Sel. Top. Power Electron.*, vol. 12, no. 2, pp. 1875–1882, 2023.
[19] W. Hu, J. Tao, Z. Ding, and H. Yang, "Analysis and control of partial power processing nonisolated bidirectional dc-dc converter," *Int. J. Circuit Theory Appl.*, vol. 51, no. 9, pp. 4427–4441, 2023.
[20] M. Z. Malik, S. Zhang, Y. Hong, A. R. A. Alwahkyan, A. Ali, and A. Farooq, "A coupled inductor-based bidirectional dc-dc converter with step-up step-down operation for electric vehicle applications," *Int. Trans. Electr. Energy Syst.*, vol. 2023, no. 1, p. 9277881, 2023.
[21] H. Shayeghi, R. Mohajery, and N. Bizon, "Analysis and implementation of a high step-up dc-dc converter integrating a hybrid voltage multiplier cell and a coupled inductor," *J. Oper. Autom. Power Eng.*, 2024.
[22] H. Shayeghi, S. Pourjafar, S. Hashemzadeh, and F. Sedaghati, "A dc-dc converter with high voltage conversion ratio recommended for renewable energy application," *J. Oper. Autom. Power Eng.*, vol. 12, no. 3, pp. 186–194, 2024.
[23] N. Bagheri, B. Tousi, and S. Alilou, "A topology of non-isolated soft switched dc-dc converter for renewable energy applications," *J. Oper. Autom. Power Eng.*, 2024.
[24] M. Biswas, H.-C. Kim, and J.-W. Park, "A coupled inductor based high step-down/step-up dc-dc nonisolated bidirectional converter with reduced ripple in current and voltage stress," *IEEE J. Emerging Sel. Top. Power Electron.*, 2024.
[25] K. Farajzadeh, L. Mohammadian, S. Shahmohammadi, and T. Abedinzadeh, "A novel bidirectional dc–dc converter with high voltage conversion ratio and capability of cancelling input current ripple," *IET Power Electron.*, vol. 17, no. 3, pp. 375–393, 2024.